A Machine Learning Emulator for Forecasting Equatorial Spread F

Aaron Kirchman[1]*, David Hysell[1], Susan Palacios[2]

[1]Department of Earth & Atmospheric Sciences, Cornell University, Ithaca, NY

[2]Section of Electricity & Electronics, Department of Engineering, Pontificia Universidad Católica del Peru, Lima, Peru

*ajk335@cornell.edu

Summary

- A regional, numerical simulation that accurately produces equatorial spread F (ESF) activity on a night-to-night basis is too computationally expensive to serve as a nowcast or forecast, motivating the development of a machine learning emulator.
- Newly implemented **Medium Power ISR (MPISR) data from Jicamarca Radio Observatory (JRO) allows for near continuous observation of plasma drifts.** 67 nights of simulations driven with MPISR drifts form a training dataset for the emulator.
- **Dimensionality reduction (CAE) and time series forecasting (LSTM) models are paired** to predict time series in a reduced dimensional latent space.
- **Emulator estimates of ESF activity show qualitative and quantitative accuracy across 30-60 minutes with over 40,000× speedup in evaluation time relative to the simulation.**

Regional Simulation

A regional, three-dimensional, data-driven simulation [1] has been used to replicate plasma density irregularities associated with ESF . **Simulation results have shown accurate estimates when compared to radar or satellite data** [1,2]. Computations include a finite-volume solver, and linear potential solver:

$$\frac{\partial n_s}{\partial t} + \nabla \cdot (n_s \mathbf{v}_s) = P_s - L_s$$

$$\mathbf{v}_s = \mu_s \cdot (\mathbf{E}_0 - \nabla\phi + \mathbf{u} \times \mathbf{B}) + \mathbf{T}_s \cdot \mathbf{g} - \mathbf{D}_s \cdot \nabla \ln(n_s)$$

$$\nabla \cdot (\sigma \cdot \nabla\phi) = \nabla \cdot \left[\sigma \cdot (\mathbf{E}_0 + \mathbf{u} \times \mathbf{B}) - \sum (q_s \mathbf{D}_s \cdot \nabla n_s) + \Xi \cdot \mathbf{g}\right]$$

JRO's new MPISR mode observes plasma drifts nearly every night. 67 nights of data from late 2023 have been used to drive the simulation. Results will act as training data for the more efficient emulator.

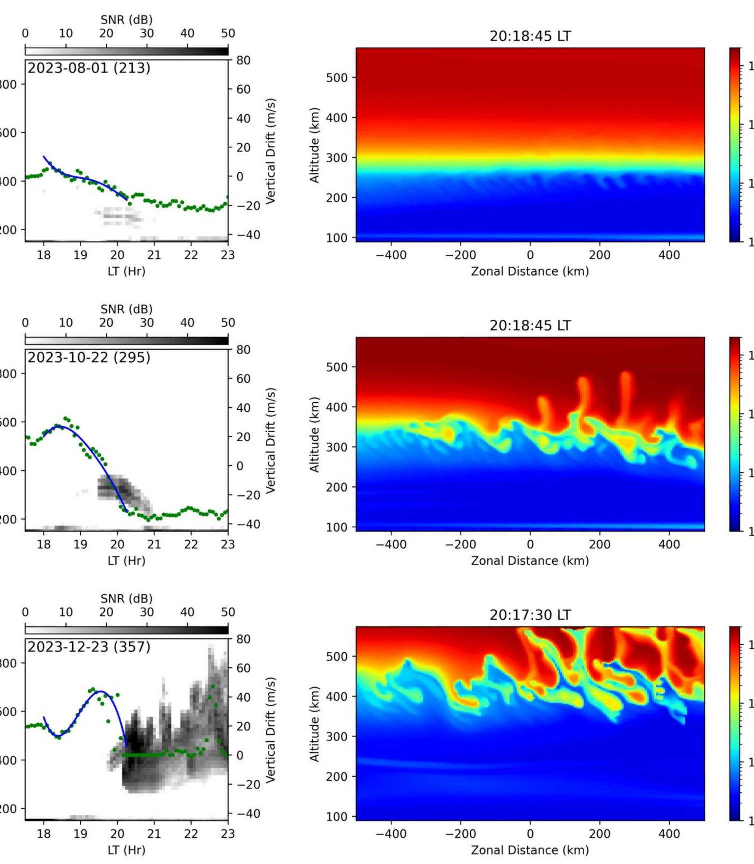

Figure 1: Comparison of radar observations and simulated electron densities in the equatorial plane.

Emulator Outline

The emulator model consists of two individual components that are coupled together during evaluation. First, **a Convolutional Autoencoder (CAE) is used to perform dimensionality reduction** on simulated electron densities, transforming to a latent space. Principal Component Analysis (PCA) was also utilized, but results were worse (see Dimensionality Reduction section). Next, **a Long-Short-Term Memory (LSTM) recurrent neural network is used to perform time series forecasting** in the latent space. Similarly structured emulators for global thermosphere models have shown recent success [3,4].

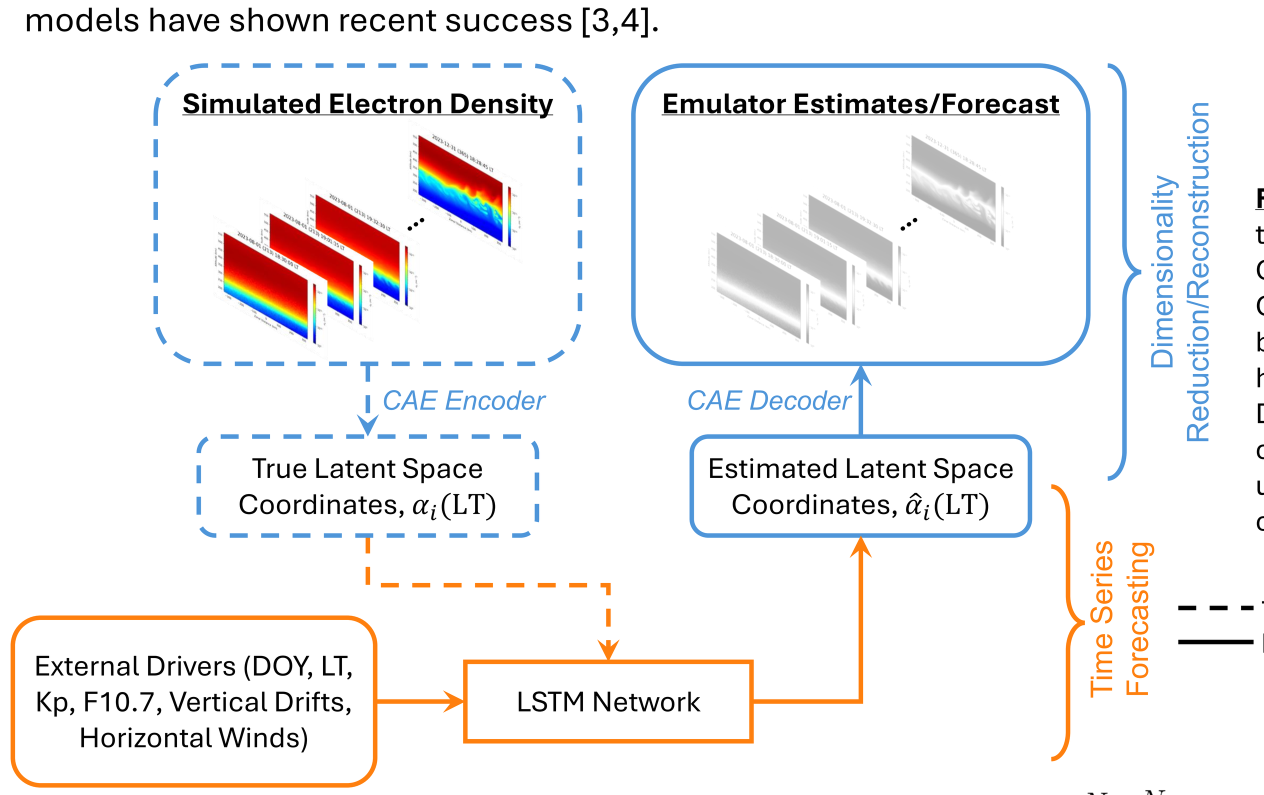

Figure 2: Schematic of the emulator. Components of the CAE are highlighted in blue, while the LSTM is highlighted in orange. Dashed lines and boxes correspond to sections used during training only.

Accuracy is quantified by weighing two error metrics:

- **Mean Relative Error (MRE)**: pixel-by-pixel error.
- **Structural Similarity Index Measure (SSIM)**: similarity measure of two image signals, composed of luminance, contrast, and structure scores [5].

$$\mathrm{MRE} = \frac{1}{N_x N_T} \sum_{i=0}^{N_x} \sum_{k=0}^{N_T} \frac{|n(x_i, t_k) - \tilde{n}(x_i, t_k)|}{n(x_i, t_k)}$$

$$\mathrm{SSIM}(y, z) = l(y, z) c(y, z) s(y, z)$$

$$l(y, z) = \frac{2\mu_y \mu_z + C_1}{\mu_y + \mu_z + C_1} \qquad c(y, z) = \frac{2\sigma_y \sigma_z + C_2}{\sigma_y + \sigma_z + C_2}$$

$$s(y, z) = \frac{\sigma_{yz} + C_3}{\sigma_y \sigma_z + C_3}$$

Dimensionality Reduction

Both principal component analysis (PCA) and a convolutional autoencoder (CAE) were tested for **reducing to a 20-dimensional latent space.**

The CAE reliably produces more accurate reconstructions, particularly capturing fine details of irregularities.

Due to its linearity, **PCA fails to capture steep density gradients**, which are the primary nonlinear feature of interchange instabilities responsible for ESF [6].

The remainder of results shown utilize the CAE.

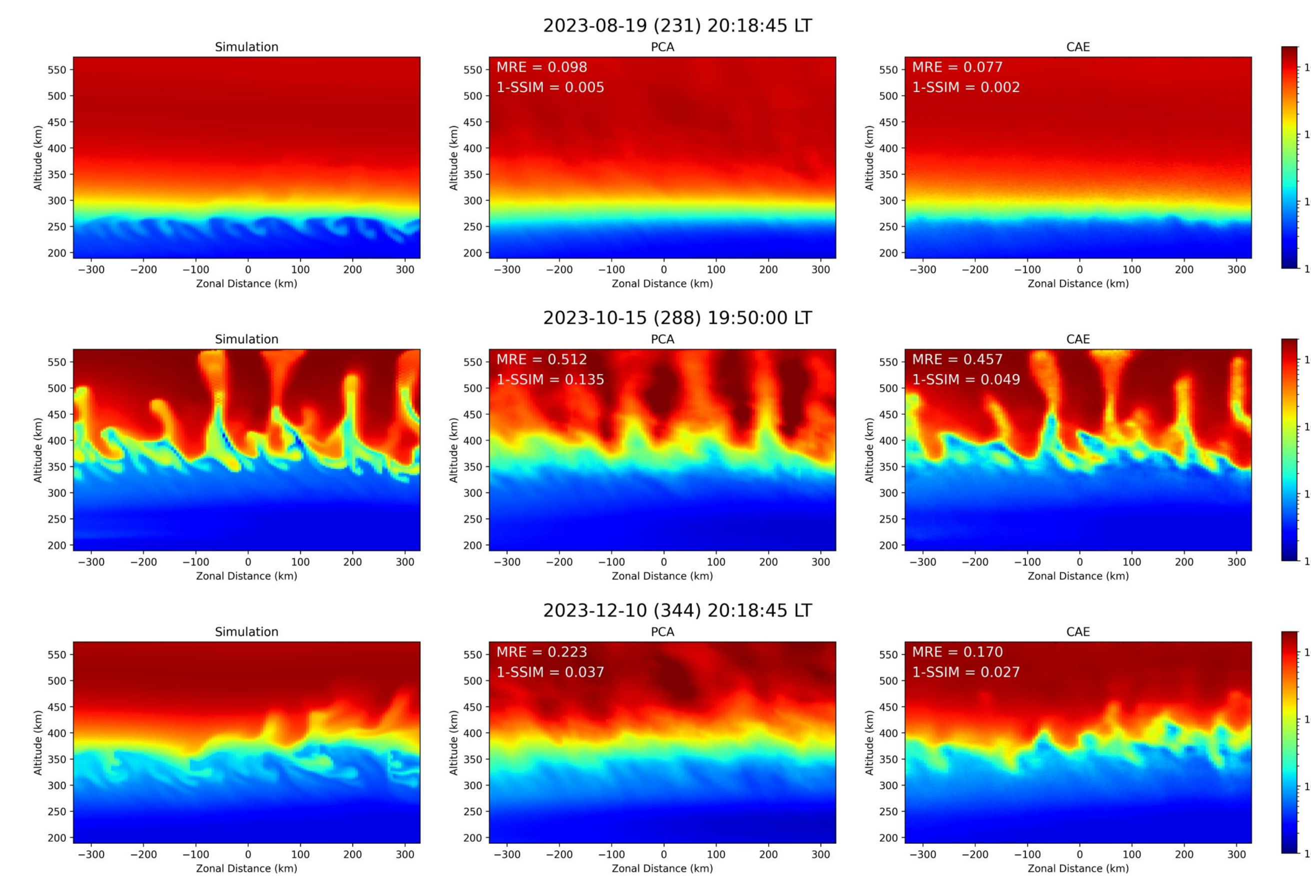

Figure 3: Comparison between simulations (left), PCA reconstructions (middle), and CAE reconstructions (right), for three test nights with differing levels of ESF activity.

	PCA				CAE			
Error Metric	Train	Validate	Test	Test (no Oct. 20)	Train	Validate	Test	Test (no Oct. 20)
MRE	0.174	0.204	0.279	0.133	0.060	0.072	0.411	0.102
1-SSIM	0.030	0.036	0.039	0.023	0.005	0.006	0.035	0.011

Table 1: Dimensionality reduction reconstruction errors. October 20 was an outlier date with particularly strong ESF.

LSTM Time Series Forecasting

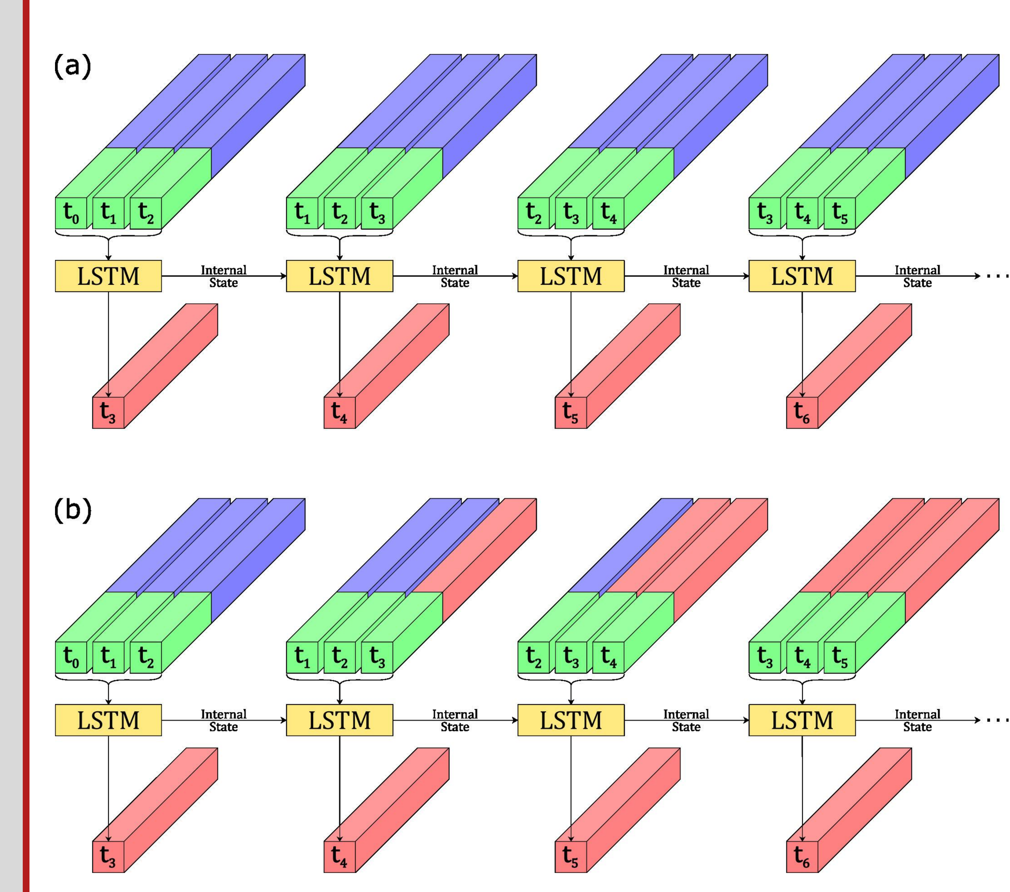

Figure 6: LSTM operation schematics for both (a) one step training, and (b) dynamic evaluation. Green, blue, and red boxes denote external drivers, true latent space values, and estimated latent space values, respectively.

An LSTM is used for time series forecasting in the latent space. Using a window of the previous N_{WS} time steps of latent space values and external drivers it estimates the latent values at the next time step. We use $N_{WS} = 5$ (6.25 minutes) and external drivers that are comparable to the inputs used in the simulation: DOY, LT, Kp, F10.7, Vertical Drifts, and Horizontal Winds.

- **One Step Training/Evaluation:** True latent values are always used for predictions (Fig. 6a). This is optimal for training, but not comparable to forecast evaluations.
- **Dynamic Training/Evaluation:** Estimated latent values are autoregressively used in future predictions (Fig. 6b). This was found to be unstable due to error accumulation when used as a training algorithm.

We introduce a new "noisy training" algorithm in which the true latent values are injected with Gaussian noise. The model is then trained in a one step fashion with noisy latent values. This procedure forces the model to learn to correct its own faults, limiting error accumulation.

Results

Fig. 5 shows emulator results for August 19, when no ESF (or only bottom-type irregularities) was observed. Temporal patterns of latent dimensions are generally captured by both evaluation strategies. No irregularities are produced in the topside. Errors remain low, with **the dynamic evaluation showing the largest error, likely due to error accumulation.** Interestingly, the dynamic evaluation best captures the small tilted wavefronts indicative of bottom-type irregularities [7].

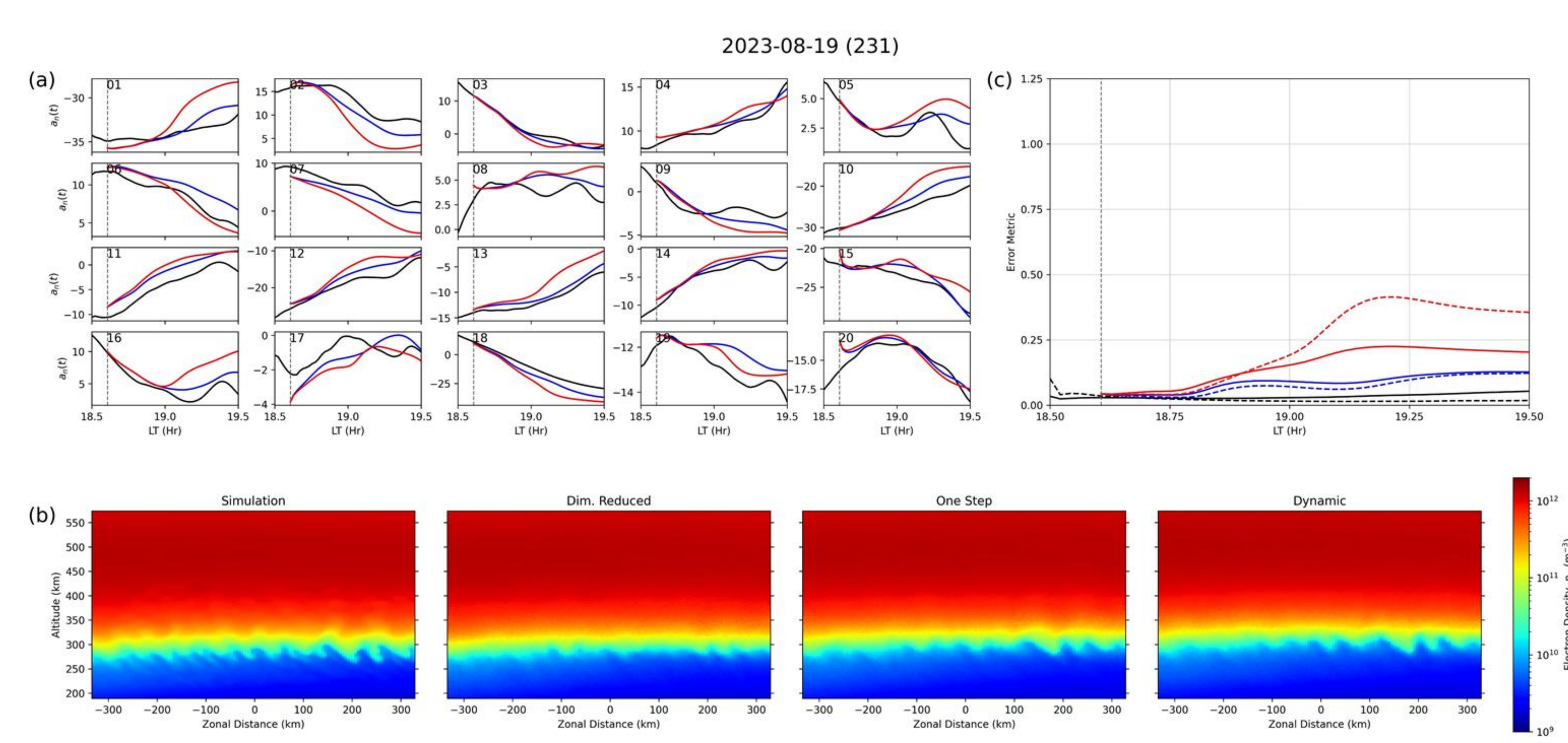

Figure 5: Results of the CAE-LSTM emulator for August 19, no ESF. (a) Latent space time series with black, blue, and red curves representing true, one step estimates, and dynamic estimates, respectively. (b) From left to right: simulation results, true CAE reconstruction, one step estimate reconstruction, dynamic estimate reconstruction. (c) MRE (solid) and $10 \times (1 - SSIM)$ (dashed) errors for true reconstructions, one step estimates, and dynamic estimates.

Fig. 6 shows emulator results for October 15, when topside irregularities were observed. Dynamic evaluation fails to produce rapid fluctuations in latent space time series suggesting the LSTM acts as a regulator. **Estimated irregularities are clear and are produced at the correct zonal locations but are approximately 50-100km shorter than those observed and simulated.** All errors tend to grow beyond approximately 40 minutes suggesting **dimensionality reduction is the primary error source for topside ESF events.**

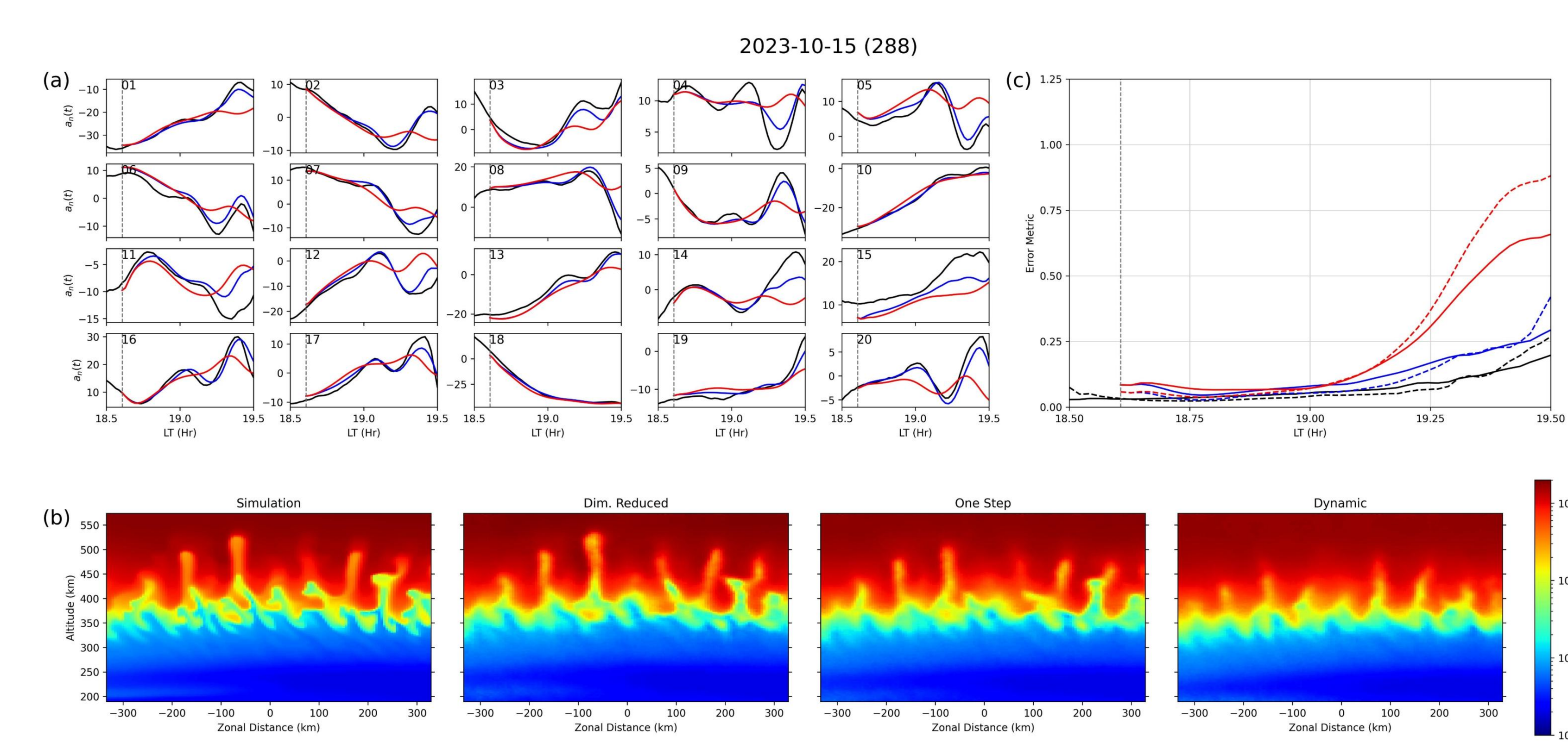

Figure 6: Results of the CAE-LSTM emulator for October 15, topside ESF. Same layout as Figure 5.

Conclusions & Future Work

- Nonlinear dimensionality reduction is necessary to capture nonlinear features of ESF irregularities.
- Dynamic evaluation produces **reasonable 30-60 minute forecasts/nowcasts of ESF development and relative intensity.**
- Emulator estimates are **evaluated in approximately 2 seconds, providing over 40,000× speedup.**
- Larger training datasets are currently being developed using 2024-2026 MPISR observations.
- Improved autoregressive time series forecasting will greatly benefit the model.
- **Limited persistence of the PRE [8] may be a major roadblock in providing vertical drifts as a driver of the emulator.**

References

[1] Hysell, D. L., Jafari, R., Milla, M. A., & Meriwether, J. W. (2014). Data-driven numerical simulations of equatorial spread F in the Peruvian sector. *Journal of Geophysical Research: Space Physics*, *119*(5), 3815–3827.

[2] Hysell, D. L., Kirchman, A., Harding, B. J., Heelis, R. A., England, S. L., Frey, H. U., & Mende, S. B. (2024). Using ICON Satellite Data to Forecast Equatorial Ionospheric Instability Throughout 2022. *Space Weather*, *22*(3), e2023SW003817.

[3] Licata, R. J., & Mehta, P. M. (2023). Reduced Order Probabilistic Emulation for Physics-Based Thermosphere Models. *Space Weather*, *21*(5), e2022SW003345.

[4] Mehta, P. M., & Licata, R. J. (2025). TIE-GCM ROPE - Dimensionality Reduction: Part I. *Space Weather*, *23*(1), e2024SW004185.

[5] Wang, Z., Simoncelli, E. P., & Bovik, A. C. (2003). Multiscale structural similarity for image quality assessment. *The Thirty-Seventh Asilomar Conference on Signals, Systems & Computers, 2003*, 1398–1402.

[6] Zargham, S., & Seyler, C. E. (1989). Collisional and inertial dynamics of the ionospheric interchange instability. *Journal of Geophysical Research: Space Physics*, *94*(A7), 9009–9027.

[7] Hysell, D. L., & Kudeki, E. (2004). Collisional shear instability in the equatorial F region ionosphere. *Journal of Geophysical Research: Space Physics*, *109*(A11).

[8] Kirchman, A., & Hysell, D. L. (2025). Persistence of the Prereversal Enhancement of the Equatorial Vertical Plasma Drifts Observed by ICON. *Geophysical Research Letters*, *52*(20), e2025GL118390.